

# Hydrogen Release from Mixtures of Lithium Borohydride and Lithium Amide: A Phase Diagram Study

Gregory P. Meisner,<sup>\*,†</sup> Matthew L. Scullin,<sup>‡</sup> Michael P. Balogh,<sup>‡</sup> Frederick E. Pinkerton,<sup>†</sup> and Martin S. Meyer<sup>†</sup>

General Motors Research and Development Center, Warren, Michigan 48090-9055

Received: October 20, 2005; In Final Form: December 15, 2005

We recently reported the synthesis of a new quaternary hydride in the lithium–boron–nitrogen–hydrogen quaternary phase diagram with the approximate composition  $\text{LiB}_{0.33}\text{N}_{0.67}\text{H}_{2.67}$  having a theoretical hydrogen content of 11.9 wt %. This new compound forms by the reaction of appropriate amounts of lithium amide ( $\text{LiNH}_2$ ) and lithium borohydride ( $\text{LiBH}_4$ ) and releases greater than 10 wt % hydrogen when heated. A small amount of ammonia, 2–3 mol % of the generated gas, is also released. We now report a study of hydrogen and ammonia release from the series of reactant mixtures  $(\text{LiNH}_2)_x(\text{LiBH}_4)_{1-x}$ , where  $x = 0.667$  corresponds to the composition  $\text{LiB}_{0.33}\text{N}_{0.67}\text{H}_{2.67}$ . We measured hydrogen and ammonia release amounts as a function of composition and found that maximum hydrogen and minimum ammonia release do occur for  $x = 0.667$ . We also present evidence for an additional new quaternary phase and for two possibly metastable phases in this system.

## Introduction

Research on hydrogen storage is focused on new substances having large gravimetric and volumetric hydrogen densities plus fast sorption kinetics at practical temperatures and pressures.<sup>1</sup> Ideally, these substances should also be durable, inexpensive, and safe. Among the materials studied for hydrogen storage are metal hydrides,<sup>2,3</sup> physisorptive materials<sup>4–8</sup> such as high-surface area carbon-based cryoadsorbents, and hydrogen compounds such as the alanates<sup>9–13</sup> and borohydrides.<sup>14</sup> Unfortunately, no known substance meets all of the technical requirements for a practical lightweight, large capacity, convenient hydrogen storage system for vehicles. Implementation of hydrogen powered fuel cells on automobiles still requires a technological breakthrough in practical on-board hydrogen storage. We are therefore continuing to study materials formed with light elements and large hydrogen contents.

We observed previously<sup>15</sup> that among the many well-studied hydrogen storage materials involving various combinations of lightweight hydrogen-containing compounds, not all of the stored hydrogen is released at practical temperatures and pressures. We were motivated, therefore, to look for substances and for reactions between substances with hypothetical hydrogen desorption reactions having hydrogen-free end products, and in this way find a material that fully releases and cycles all of the stored hydrogen. The existence of the ternary compound  $\text{Li}_3\text{BN}_2$ <sup>16–21</sup> suggested the possible reaction  $2\text{LiNH}_2 + \text{LiBH}_4 \rightarrow \text{Li}_3\text{BN}_2 + 4\text{H}_2$ , which would release 11.9 wt % of  $\text{H}_2$ . Not only does this reaction occur,<sup>22</sup> but we found a previously unknown quaternary hydride with a body-centered cubic structure, lattice constant  $a = 10.76 \text{ \AA}$ , and the approximate composition  $\text{LiB}_{0.33}\text{N}_{0.67}\text{H}_{2.67}$ . We previously referred to this as “ $\text{Li}_3\text{BN}_2\text{H}_8$ ”<sup>22</sup> and hereafter denote it as the  $\alpha$  phase. Recent

X-ray diffraction results<sup>23</sup> on single crystals of this body-centered cubic  $\alpha$  phase reveal, however, that its true equilibrium composition is  $\text{Li}_4\text{BN}_3\text{H}_{10}$ .

We previously showed<sup>22</sup> that the  $\alpha$  phase readily forms by either ball milling the reactants for 300 min or mixing the individually ball milled reactants and heating to  $\sim 95^\circ\text{C}$ . When heated, this material melts at  $\sim 195^\circ\text{C}$ , and above  $250^\circ\text{C}$ , it exothermically releases  $\geq 10$  wt % of hydrogen and a small amount (2–3 mol %) of ammonia. To determine the optimum stoichiometry for hydrogen release in terms of temperature, pressure, and ammonia content, we investigated the accessible portion of the Li–B–N–H phase diagram using mixtures of  $\text{LiBH}_4$  and  $\text{LiNH}_2$ .

## Experimental Details

We prepared mixtures of  $\text{LiBH}_4$  and  $\text{LiNH}_2$  from commercially available powders ( $\text{LiNH}_2$ : Aldrich, 95% purity; and  $\text{LiBH}_4$ : Lancaster, 95% purity) handled in an inert atmosphere (Ar) glovebox, described previously.<sup>22</sup> For *ball milled* samples, we put 1 g of powder mixtures plus one large (1.27 cm diameter) and two small (0.635 cm diameter) steel balls into O-ring sealed, hardened steel ball mill jars. Samples were milled with a SPEX 8000 Mixer/Mill for 300 min. Mixtures of  $\text{LiNH}_2$  and  $\text{LiBH}_4$  of the form  $(\text{LiNH}_2)_x(\text{LiBH}_4)_{1-x}$  were synthesized for compositions  $x = 0.33, 0.50, 0.556, 0.60, 0.636, 0.667, 0.692, 0.75$ , and  $0.80$ . We recovered white powders from the ball mill jars after 300 min of ball milling except for compositions  $x = 0.556, 0.60$ , and  $0.636$ , which we recovered as a dark solid clump, presumably a result of the reacted powders melting in the ball mill jar. For the *mixed* samples, 1 g each of  $\text{LiBH}_4$  and  $\text{LiNH}_2$  were separately ball milled for 10 min, combined in appropriate amounts totaling 1 g, and then intimately mixed by processing for another 10 min in the ball mill jar with the balls removed.

We performed temperature-dependent in situ X-ray diffraction (XRD) experiments using a Bruker AXS General Area Detector Diffractometer System (GADDS).<sup>11</sup> Quartz capillary tubes were loaded with powders under Ar and then transported to the

\* To whom correspondence should be addressed. E-mail: gregory.p.meisner@gm.com.

<sup>†</sup> Materials and Processes Laboratory.

<sup>‡</sup> Chemical and Environmental Sciences Laboratory.

diffractometer in a sealed fixture. We used a 0.8 mm collimator and a detector distance of 15 cm, with the center of the sample cell at angles  $\Omega = 0^\circ$  and  $2\theta = 27^\circ$ , and integrated the observed Debye rings to give powder XRD patterns for angles  $9.6^\circ \leq 2\theta \leq 41.5^\circ$ . We recorded pressure and temperature as samples were heated from room temperature to  $T > 300^\circ\text{C}$  at  $2^\circ\text{C}/\text{min}$ , and a full XRD pattern was collected every 150 s.

We performed volumetric measurements<sup>7</sup> using the Advanced Materials Corporation's Gas Reaction Controller (GRC) described previously.<sup>10</sup> The amount of  $\text{H}_2$  gas released into the evacuated sample chamber was determined by measuring temperature and pressure while heating the sample to  $350^\circ\text{C}$  at  $2^\circ\text{C}/\text{min}$ . The final amount of gas evolved was determined only after the sample was cooled and the experiment reached equilibrium conditions at  $25^\circ\text{C}$ . Typically, the thermal desorption experiment evolved about 1200 KPa of gas pressure in the sample chamber.

The gas desorbed in the GRC experiments was bubbled through water and tested for ammonia with the Merck EM Quant of Gibbstown, NJ, Ammonia Test kit, catalog no. 10024-1. Ten drops of sodium hydroxide solution from the kit were placed in 5 mL of the test water and test strips were held in the water for 3 s before being removed for comparison with a color chart. A change in strip color indicated the presence of ammonia, and several strips were tested to ensure the accuracy of the kit materials, using a dilute  $\text{NH}_4^+$  solution with 10 drops of NaOH added per the instructions of the kit.

We performed ambient pressure gravimetric measurements in flowing Ar gas using a Perkin-Elmer Model TGA7 thermogravimetric analyzer (TGA) that was housed in an Ar glovebox to protect the air-sensitive samples during loading. Samples of 1 to 4 mg were sealed into Al pans whose lids have a  $50\ \mu\text{m}$  hole to permit egress of the evolved gas. The samples were heated to  $400^\circ\text{C}$  at  $5^\circ\text{C}/\text{min}$  and cooled at  $20^\circ\text{C}/\text{min}$ .

We performed high-pressure TGA with mass spectrometry using a Cahn Model 2151 thermogravimetric analyzer capable of pressures up to 100 bar and temperatures up to  $1000^\circ\text{C}$  in either flowing  $\text{H}_2$  or He gas.<sup>24</sup> Approximately 300 mg of powder was loaded into a quartz sample bucket in a glovebox. The bucket was then filled with anhydrous pentane to protect the sample from air exposure while the sample was loaded into the TGA. X-ray diffraction analysis of test samples confirmed that they were unchanged after immersion in and subsequent evaporation of the pentane. The TGA was thoroughly purged with He gas while the pentane evaporated. The sample was heated to  $350^\circ\text{C}$  in flowing He gas and held at that temperature. Gas desorption was directly measured as weight loss by the sample during heating, corrected for nongravitational forces due to gas buoyancy, gas flow velocity, and electrobalance temperature.<sup>24</sup> A differentially pumped mass spectrometer operated as a residual gas analyzer (RGA) monitored the composition of the exhaust gas. The RGA captured nine mass channels corresponding to 2 ( $\text{H}_2$ ), 4 (He), 16 (the  $\text{NH}_2^+$  gas fragment of  $\text{NH}_3$ , or  $\text{CH}_4$ ), 17 ( $\text{NH}_3$  or the  $\text{OH}^-$  radical of  $\text{H}_2\text{O}$ ), 18 ( $\text{H}_2\text{O}$ ), 26 (diborane), 28 ( $\text{N}_2$  or  $\text{CO}$ ), 32 ( $\text{O}_2$ ), and 44 ( $\text{CO}_2$ ) amu. RGA detection of gas evolved from the sample was delayed by about 3 min compared to the corresponding TGA weight loss due to the transit time of the gas flow between the TGA sample chamber and the RGA inlet.

## Results and Discussion

Consistent with our previous results on ball milling versus heating of mixed powders for  $\text{LiB}_{0.33}\text{N}_{0.67}\text{H}_{2.67}$  ( $x = 0.667$ ),<sup>22</sup> we observed that a mixture of composition  $x = 0.60$  could be

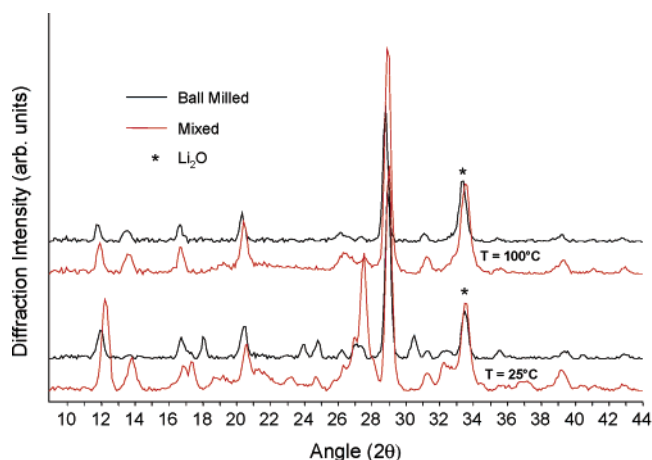


**Figure 1.** XRD data of ball milled and mixed  $(\text{LiNH}_2)_{0.60}(\text{LiBH}_4)_{0.40}$  at  $T = 25^\circ\text{C}$  and  $100^\circ\text{C}$ . The peak at  $2\theta = 33.5^\circ$  marked with an asterisk is the  $\text{Li}_2\text{O}$  impurity phase.

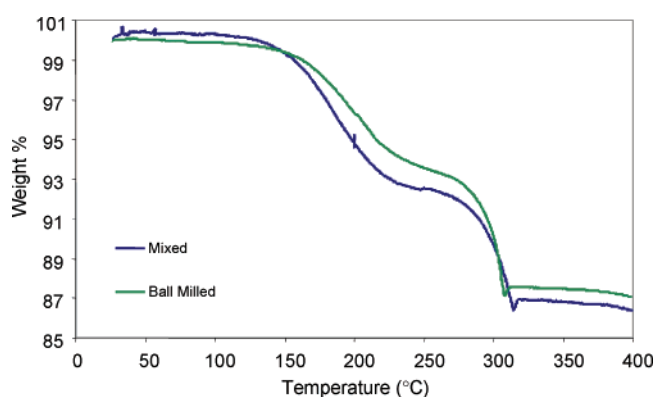


**Figure 2.** TGA desorption curves for both ball milled and mixed samples of composition  $x = 0.60$  are shown as a function of temperature. The two-step desorption behavior and total amount of released gas are essentially the same for both. The slight reduction in total weight loss for ball milled compared to mixed is consistent with a small amount of the sample decomposing during the ball milling process.

synthesized using either the milling or the mixing method. The results in Figure 1 show that the XRD data are equivalent at  $100^\circ\text{C}$ . Gas desorption properties measured by TGA, Figure 2, are also equivalent, with the ball milled sample showing  $\sim 1$  wt % less desorption than the mixed sample, presumably due to a small amount of decomposition during ball milling and accompanying melting.

The ball milled mixtures  $(\text{LiNH}_2)_x(\text{LiBH}_4)_{1-x}$  were characterized by using in situ XRD measurements. Representative XRD data versus temperature are shown in Figure 3 for  $x = 0.75$ . The lithium oxide impurity,  $\text{Li}_2\text{O}$ , is presumably due to a small amount of contamination in the starting material and/or exposure to small amounts of air sometime during sample synthesis. We note that the  $\text{Li}_2\text{O}$  diffraction peak at  $2\theta \approx 33.5^\circ$  was present throughout the experiment, indicating that the sample was always in the X-ray beam and that the disappearances of other diffraction peaks were due to phase transformations and not the sample falling or moving out of the X-ray beam. Initially, the XRD data consisted of the  $\alpha$  phase and diffraction peaks attributable to the  $\delta$  phase. As the sample was heated, peaks associated with the  $\delta$  phase ( $2\theta = 24\text{--}26^\circ$ ) vanished at  $T \sim 50^\circ\text{C}$ , suggesting melting of the  $\delta$  phase. Above  $190^\circ\text{C}$ , the background increased as the  $\alpha$  phase peaks disappeared, consistent with melting of the  $\alpha$  phase. Above  $\sim 300^\circ\text{C}$ , new diffraction lines appeared that corresponded to polymorphs of

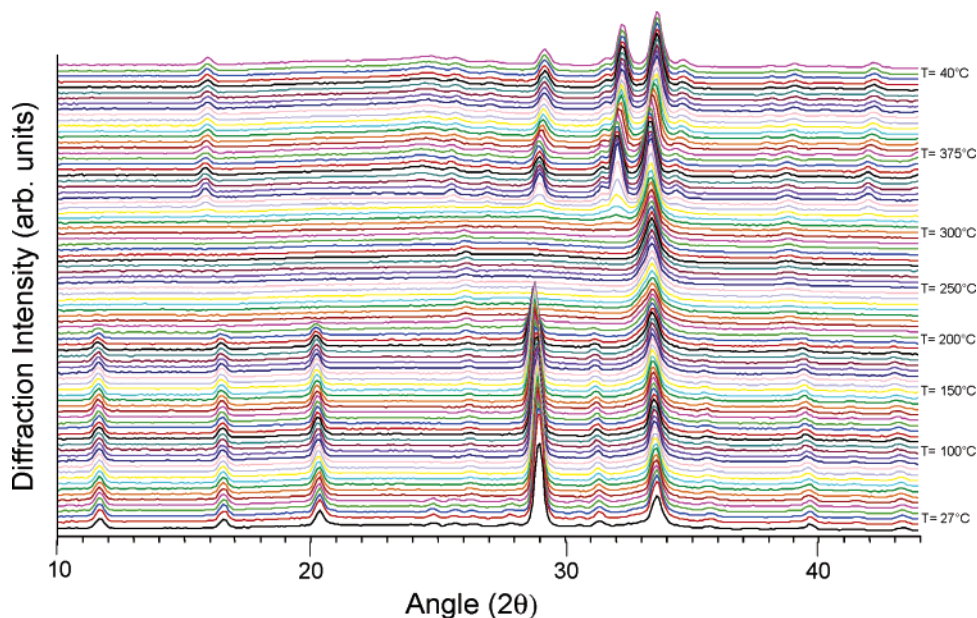


**Figure 3.** These in situ XRD data for  $x = 0.75$  were collected as the sample was heated to 375 °C and then cooled to room temperature. Note the disappearance of the diffraction peaks of the  $\alpha$  phase consistent with melting near 200 °C. The strongest peaks for the  $\delta$  phase occur for  $2\theta = 24\text{--}26^\circ$  at temperatures below  $\sim 50^\circ\text{C}$ . The peak at  $2\theta = 33.5^\circ$  is the  $\text{Li}_2\text{O}$  impurity, and peak shifts during heating and cooling are due to thermal expansion and contraction.

$\text{Li}_3\text{BN}_2$ , consistent with solidification. The background intensities are sometimes higher at the start of the experiment than at the end, which is likely due to there being less sample in the X-ray beam at the end of the experiment after the sample melted, released gas, and shifted within the capillary tube. It is also possible that some amorphous material existed in the ball milled sample at the beginning of the experiment but was not present after the thermal cycling.

These in situ XRD measurements and analysis allowed us to monitor the various phases in each sample by tracking the occurrence and disappearance of sets of diffraction peaks with composition and temperature. Our results for the various compositions are summarized in Figure 4 using the measured data at room temperature along with data for the starting materials  $\text{LiNH}_2$  and  $\text{LiBH}_4$ . From these data, plus the changes in these XRD patterns as a function of temperature, such as in Figure 3, we identified sets of peaks corresponding to three new phases  $\beta$ ,  $\gamma$ , and  $\delta$ , in addition to the previously identified<sup>22</sup> bcc  $\alpha$  phase that occurs near the composition  $x = 0.667$ . The peaks for the  $\beta$  phase at  $x = 0.50$  (see Figure 4) also indicate a bcc lattice, but with a smaller lattice constant of  $a = 10.4 \text{ \AA}$ . The large differences in relative peak intensities between the  $\alpha$  and  $\beta$  phases, however, imply different crystal structures rather than merely a shift in lattice constant. The sets of diffraction peaks we identify as the  $\gamma$  and  $\delta$  phases are shown in Figure 5; we have not yet determined the lattice symmetry for these phases.

The results for gas desorption measurements with both volumetric<sup>7</sup> and thermogravimetric<sup>24</sup> techniques are shown in Figure 6 for samples with  $x = 0.667$ , 0.60, and 0.50. The data for  $x = 0.60$  and 0.50 clearly reveal two separate desorption onsets and desorption steps whereas the corresponding volumetric curves show only one large pressure increase. This is evidence for the desorption of two gas species having significantly different molecular weights, one being  $\text{H}_2$ . Because  $\text{LiNH}_2$  decomposes by releasing  $\text{NH}_3$  under certain conditions,<sup>25,26</sup> we presumed the second desorbed gas species to be  $\text{NH}_3$ . Indeed, our qualitative analysis using an Ammonia Test Kit confirmed that the concentration of  $\text{NH}_3$  in the captured

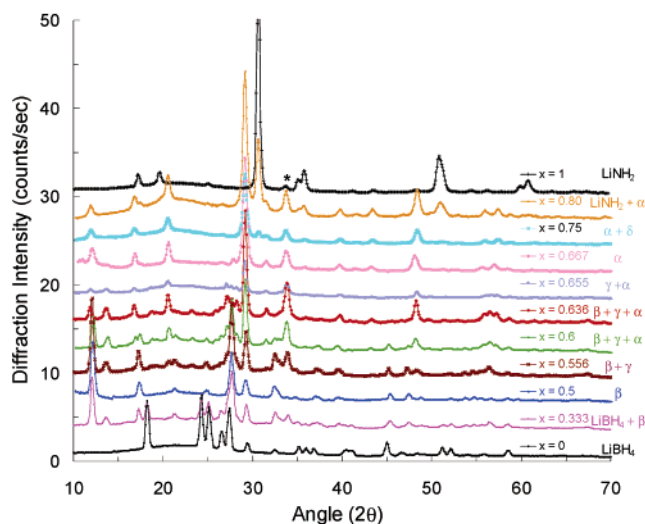


**Figure 4.** The room-temperature XRD data for ball milled samples prior to heating shows sets of peaks corresponding to four intermediate hydride phases. The compound at  $x = 0.667$  is the new quaternary hydride  $\alpha$  phase previously reported in ref 22. Another new phase, denoted  $\beta$ , occurs at  $x = 0.50$ . Additional peaks appear in the XRD data for intermediate compositions and can be associated with other distinct phases, denoted  $\gamma$  and  $\delta$ . This identification is facilitated by the tracking of diffraction peaks as a function of temperature at a given composition, such as the data in Figure 3, in addition to the room-temperature data shown here. The  $\gamma$  and  $\delta$  phases may be metastable, however, only arising from thermal or compositional nonequilibrium conditions created by ball milling. The peak at  $2\theta = 33.5^\circ$  marked with an asterisk is the  $\text{Li}_2\text{O}$  impurity.

gas from the volumetric measurements was in qualitative agreement with the sizes of the two desorption steps in the TGA curves. The desorbed gas from all samples had detectable levels of  $\text{NH}_3$  with use of the Ammonia Test Kit except for  $x = 0.667$  (and for  $x = 0.692$ , which was not tested), and mass spectrometry confirmed that the two species present in the desorbed gas were indeed  $\text{H}_2$  and  $\text{NH}_3$ .

We quantitatively determined the  $\text{H}_2$  and  $\text{NH}_3$  content of the desorbed gas using one or more of three methods. First, we



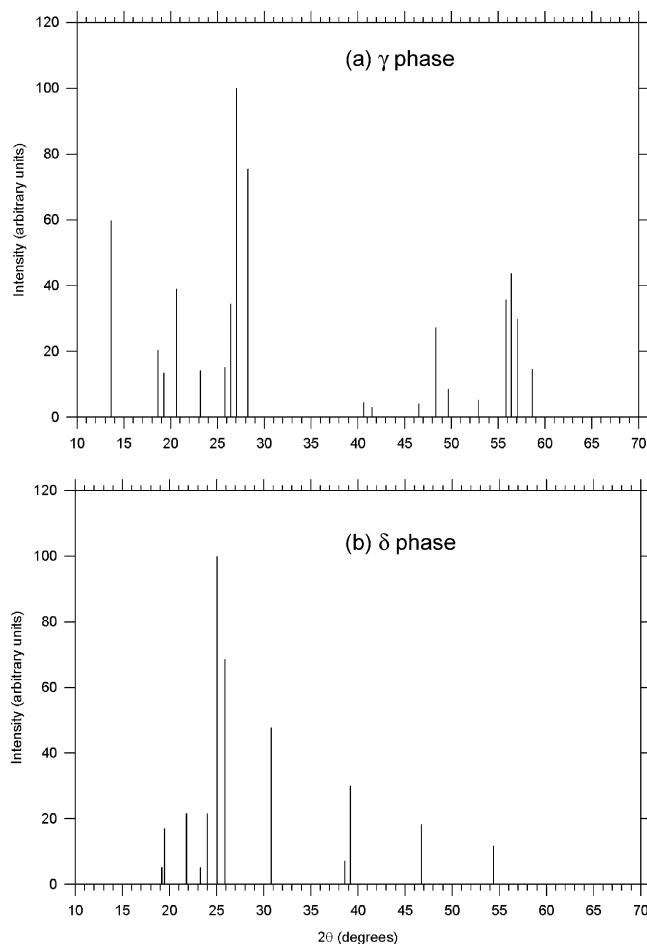


**Figure 5.** These schematic diffraction patterns are the sets of peaks we tentatively identify as the (a)  $\gamma$  phase and (b)  $\delta$  phase. We analyzed both room-temperature XRD data (Figure 4) and in situ temperature dependent XRD data (e.g., Figure 3) to determine which compositions contained these phases, and at what temperatures. This allowed us to unambiguously track these sets of peaks which occurred all together at specific compositions and then disappeared all together when the samples were heated.

computed gas compositions consistent with both volumetric measurements of the total moles of gas released and TGA measurements of the total grams of gas released.<sup>27</sup> These results are listed as (Vol/TGA) in Table 1. Second, we analyzed the two-step gas release profile of the TGA curves shown in Figure 6. Most of the gas pressure develops in the volumetric measurements at temperatures corresponding to the higher temperature mass loss step in the TGA measurements. Also, the single step in the TGA curve for  $x = 0.667$  is due to the release being almost entirely  $H_2$  as determined by the “Vol/TGA” analysis and by mass spectrometry. Hence, in the TGA measurements, the lower temperature step is due to  $NH_3$  release and the higher temperature step is due to  $H_2$ . The relative masses of the released gases corresponding to the two TGA steps give the  $NH_3$  and  $H_2$  content of the gas, and these results are listed as “TGA steps” in Table 1. Third, we performed a quantitative mass spectrometer analysis on selected samples, and the results are shown in Figure 7 and are listed as “mass spec” in Table 1. Figure 8 shows the composition dependence of the content of the desorbed gas. We observe that the minimum amount of  $NH_3$  released is near  $x = 0.667$  and that the nonmonotonic behavior of  $H_2$  and  $NH_3$  release is suggestive that other phases or phase transitions may occur in this portion of the Li–B–N–H phase diagram.

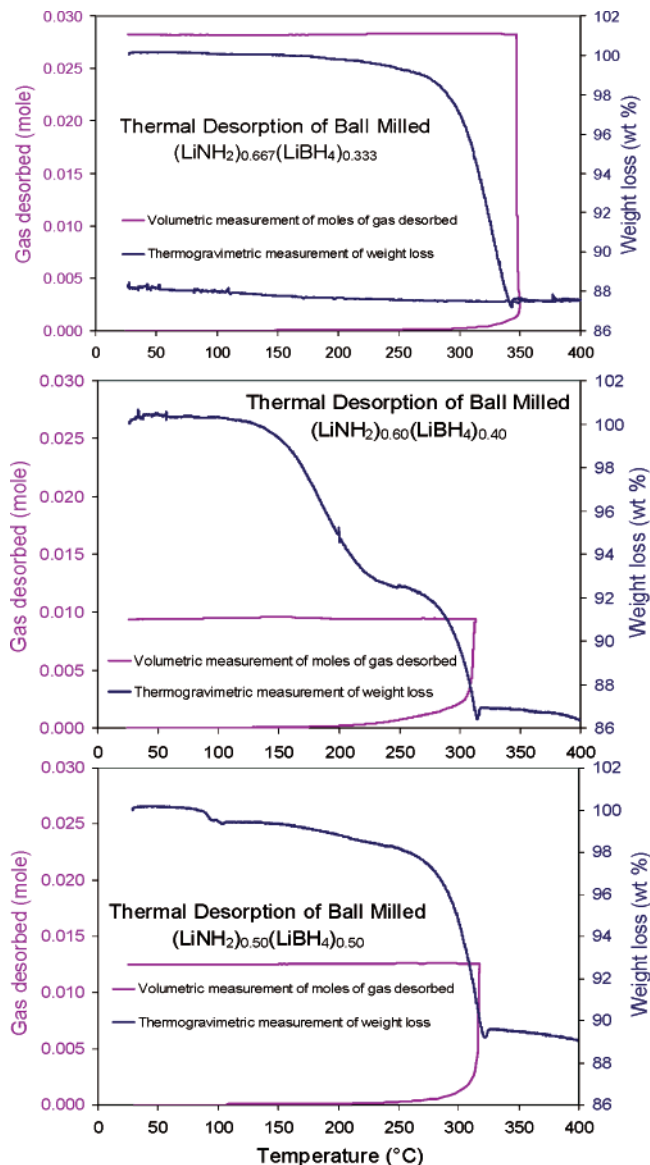


**Figure 6.** Desorption curves measured volumetrically (red) and with TGA (blue) for  $x = 0.667$ ,  $0.60$ , and  $0.50$  show that the majority of gas molecules are released at  $T > 300$  °C while mass loss occurs in two steps of variable sizes depending on composition. Our analysis confirms that  $NH_3$  is released at the lower temperatures and  $H_2$  is released near  $300$  °C (see text), and the results are listed in Table 1.

We recorded structural changes and melting for the various compositions using in situ XRD measurements<sup>11</sup> collected as a function of sample temperature. We confirmed the melting and solidification of the samples during in situ XRD experiments by visual observations using a video camera focused on the portion of the capillary tube exposed to the X-ray beam. Figure 9 shows the diffracted intensity at specific angles corresponding to significant diffraction peaks of the various phases, the background intensity at an angle well separated from any diffraction peaks, and the pressure in the capillary tube for the composition  $x = 0.75$ . The melting of the  $\alpha$  phase is quite evident at  $T \sim 200$  °C. The growth of the  $Li_3BN_2$  peaks matches the increase in pressure, clearly demonstrating that gas is released from the liquid phase which then crystallizes into  $Li_3BN_2$ . We observed this for all samples. The decrease in the  $Li_3BN_2$  peak intensity at high temperature is an artifact arising from lattice thermal expansion that caused the diffraction peak to partially shift out of the fixed  $2\theta$  window used for determining peak areas.

**TABLE 1: Hydrogen and Ammonia Gas Desorption for  $(\text{LiNH}_2)_x(\text{LiBH}_4)_{1-x}$** 

composition (x)	detection methods <sup>a</sup>	H <sub>2</sub> desorbed (wt %)	NH <sub>3</sub> desorbed (wt %)	total TGA wt loss (wt %)
0.333	Vol/TGA	4.4	2.6	7.0
	TGA steps	4	3	
0.500	Vol/TGA	8.2	2.0	10.2
	TGA steps	8.2	2.0	
0.556	TGA steps	5.6	4.0	9.6
0.600	Vol/TGA	6.6	5.6	12.2
	TGA steps	5.5	6.7	
	mass spec	6.4	5.8	
0.636	TGA steps	6	9	15.0
0.667	Vol/TGA	11.0	1.6	12.6
	TGA steps	12.6	~0	
	mass spec	11.0	1.6	
0.692	Vol/TGA	11.0	1.1	12.1
	TGA steps	12.1	~0	
	mass spec	9.7	2.4	
0.750	mass spec	9.6	8.4	18.0
0.800	mass spec	8.0	13.6	21.6

<sup>a</sup> Vol/TGA: the moles desorbed measured volumetrically and grams desorbed measured gravimetrically were used to solve for H<sub>2</sub> and NH<sub>3</sub> content. TGA steps: the sizes of desorption steps measured gravimetrically were used to determine H<sub>2</sub> (higher temperature step) and NH<sub>3</sub> (lower temperature step) content. Mass spec: the H<sub>2</sub> to NH<sub>3</sub> ratio was measured by mass spectrometry and scaled to give the total weight loss determined by the TGA measurement.

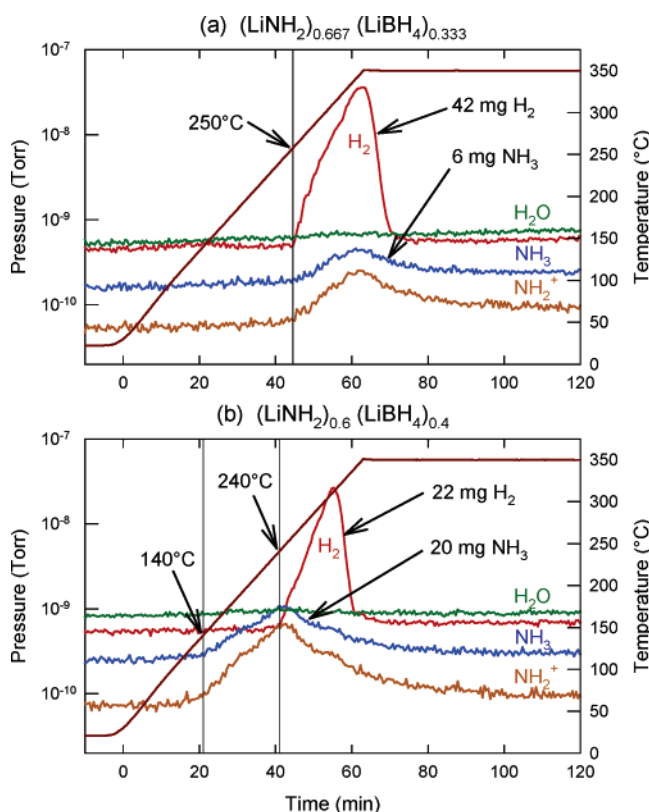


**Figure 7.** Mass spectrometry results on the gas released during high-pressure TGA experiments for  $x = 0.667$  (a) and  $0.60$  (b). This confirms that for  $x = 0.667$  the released gas is almost entirely H<sub>2</sub>, whereas for  $x = 0.60$  it contains nearly equal amounts of NH<sub>3</sub> and H<sub>2</sub> by mass, with NH<sub>3</sub> being released at a temperature nearly 100 °C lower than H<sub>2</sub>. Only background levels of H<sub>2</sub>O (shown) and N<sub>2</sub>, CO, and CO<sub>2</sub> (not shown) were detectable in these experiments.

We analyzed the in situ XRD results as a function of composition and gas desorption and mapped out phase transformations occurring for each composition as a function of temperature. Although many of the phases and phase transitions

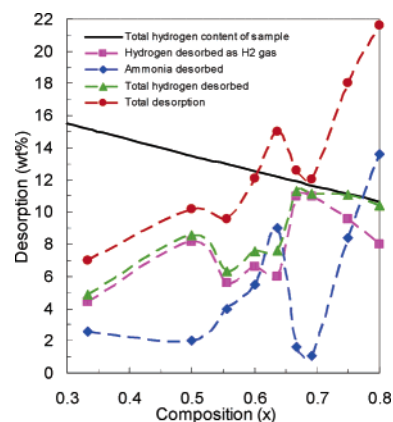


**Figure 8.** The H<sub>2</sub> content (purple squares) and NH<sub>3</sub> content (blue diamonds) of the desorbed gas determined by (Vol/TGA) analysis is plotted versus sample composition. The maximum H<sub>2</sub> release and minimum NH<sub>3</sub> release occur near  $x = 0.667$ . The red circles are the total weight loss due to both H<sub>2</sub> and NH<sub>3</sub> desorption, and the black line is the total hydrogen content of the samples versus composition. Clearly more weight is lost for  $x \geq 0.636$  than can be accounted for by H<sub>2</sub> release alone. The green triangles are the total hydrogen content of the H<sub>2</sub> and NH<sub>3</sub> in the desorbed gas, and it is always less than the total hydrogen in the samples before desorption, as expected. The dashed lines are only guides for the eye.

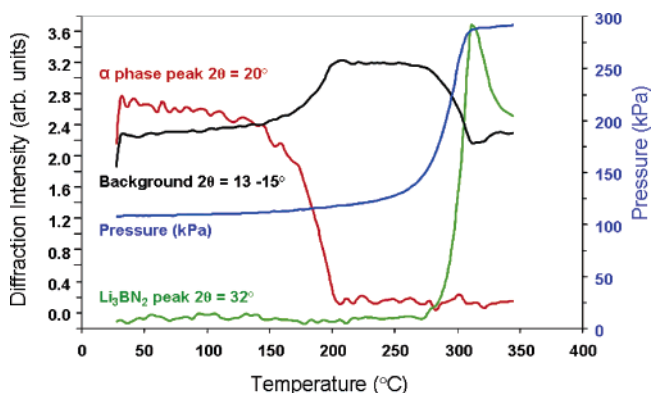


**Figure 9.** The diffraction peak intensities and the capillary tube pressure are plotted versus temperature,  $T$ , for  $x = 0.75$ . The  $\alpha$  phase melts at  $T \sim 200$  °C corresponding to the loss of diffraction intensity (red curve); the diffraction intensity at  $2\theta = 20^\circ$  for  $T$  below 200 °C is in the form of a Bragg peak, whereas for  $T$  above 200 °C it is only the background level at  $2\theta = 20^\circ$ . Melting also corresponds to an increase in the overall background levels (black curve) measured in the range  $2\theta = 13-15^\circ$  where no Bragg peaks are observed. For  $T > 300$  °C, the attenuation of the background (black curve) and the growth of the Li<sub>3</sub>BN<sub>2</sub> peaks (green curve) match the rise in pressure (blue curve), clearly demonstrating that gas is released from the liquid phase, which then crystallizes into Li<sub>3</sub>BN<sub>2</sub>. We observed this for all samples.

we have studied here are definitely not occurring under equilibrium conditions, it is nevertheless useful to capture our results in a nonequilibrium phase diagram. The result, shown in Figure 10, is based on our XRD data collected for the compositions  $x = 0.333, 0.50, 0.556, 0.60, 0.667, 0.75$ , and  $0.80$ , and the desorption results listed in Table 1. Because the number of compositions studied is small, the locations of the phase boundaries are approximate, and those boundaries with dotted lines are speculative. Sample compositions for  $x \leq 0.667$  exhibit multiple melting transitions: the diffraction peaks of the  $\gamma$  phase disappear at  $T \sim 45$  °C, the  $\beta$  phase melts, and the samples become the  $\alpha$  phase plus liquid in the range  $T = 75-90$  °C (circles), and the  $\alpha$  phase melts in the range  $T = 150-190$  °C (diamonds). At  $x = 0.75$ , the  $\delta$  phase disappears at  $\sim 50$  °C and then the  $\alpha$  phase melts at 190 °C. The NH<sub>3</sub> and H<sub>2</sub> release

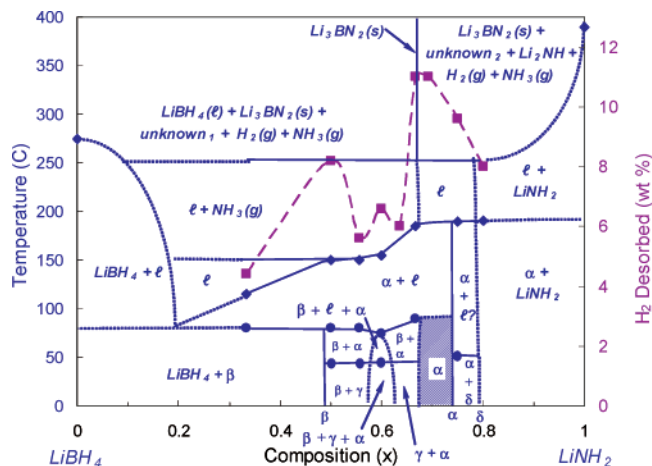


**Figure 10.** A nonequilibrium phase diagram for the  $(\text{LiNH}_2)_x(\text{LiBH}_4)_{1-x}$  system constructed from room-temperature XRD data (Figure 4) plus results from TGA and in situ XRD experiments. Plotted are melting temperatures (diamonds for the  $\alpha$  phase and circles for all other phases), based on in situ XRD data, and  $\text{H}_2$  and  $\text{NH}_3$  desorption temperatures (solid horizontal lines at 250 and 165 °C) and wt %  $\text{H}_2$  desorbed (squares), based on TGA data. Dotted lines are speculative. The XRD data have evidence for the  $\gamma$  phase at  $x = 0.60, 0.636$ , and  $0.667$ , and the  $\delta$  phase at  $x = 0.8$ , in the as-prepared samples, but because these are ball milled materials, the  $\gamma$  and  $\delta$  phases may not occur in a true equilibrium phase diagram. Similarly, the extended homogeneity range of the  $\alpha$  phase may also be a nonequilibrium effect.

behaviors determined from TGA measurements are also indicated. In addition, we have plotted in Figure 10 the amount of hydrogen desorbed as  $\text{H}_2$  (squares) as a function of composition. Note that the local maxima in the amount of desorbed  $\text{H}_2$  correlates with the estimated compositions of the observed  $\alpha$ ,  $\beta$ , and  $\gamma$  phases. In the mixed phase regions, however, a larger fraction of the desorbed hydrogen is in the form of  $\text{NH}_3$ , and this shifts the sample composition toward the  $\text{LiBH}_4$  side of the phase diagram, whereas pure  $\text{H}_2$  desorption does not.

Figure 10 illustrates how the presence of the different phases influences the type and amount of gas released when the material is heated, but it does not capture the effect of heating rates, reaction rates, and other kinetic effects. This is because all the measurements were performed at a limited number of heating rates: 2 °C/min for volumetric and XRD and 5 °C/min for TGA and mass spectrometry. If heating is done more slowly, there would be more time for  $\text{NH}_3$  release before the temperature is high enough for  $\text{H}_2$  release. At higher heating rates, the temperature for  $\text{H}_2$  release is reached sooner, at which point the release of  $\text{H}_2$  is faster than that of  $\text{NH}_3$ , and once all of the  $\text{H}_2$  is released at higher temperatures, no more  $\text{NH}_3$  can be released. Finally, we observe that the optimum composition for maximum  $\text{H}_2$  and minimum  $\text{NH}_3$  release is  $x = 0.667$ . This implies that the composition of the decomposition product,  $\text{Li}_3\text{BN}_2$ , plays the dominant role in the  $\text{H}_2$  versus  $\text{NH}_3$  release from this material rather than the composition of the crystalline phase  $\text{Li}_4\text{BN}_3\text{H}_{10}$ . Indeed, because the gas release occurs from the liquid phase, it is apparent that  $\text{Li}_3\text{BN}_2\text{H}_8$  is the liquid phase composition that would give only  $\text{H}_2$  release and form  $\text{Li}_3\text{BN}_2$ , whereas the composition  $\text{Li}_4\text{BN}_3\text{H}_{10}$  has extra nitrogen. In the latter case, the decomposition is expected to be  $\text{Li}_4\text{BN}_3\text{H}_{10} \rightarrow \text{Li}_3\text{BN}_2 + \frac{1}{2}\text{Li}_2\text{NH} + \frac{1}{2}\text{NH}_3 + 4\text{H}_2$ . In the presence of  $\text{H}_2$ , any amides or imides that form during decomposition can ultimately decompose to  $\text{LiH}$  and  $\text{NH}_3$ .<sup>25,26</sup>

## Conclusions

Our study of hydrogen storage materials of the composition  $(\text{LiNH}_2)_x(\text{LiBH}_4)_{1-x}$  formed by ball milling reactant mixtures shows two distinct crystalline body-centered cubic (bcc) phases at room temperature. The  $\alpha$  phase has a bcc structure with lattice constant  $a = 10.76$  Å. This our previously identified new quaternary hydrogen generation material and corresponds to the structure of  $\text{Li}_4\text{BN}_3\text{H}_{10}$ .<sup>23</sup> The  $\beta$  phase, at  $x \approx 0.5$ , also has a cubic lattice with  $a = 10.4$  Å, but has significantly different peak intensities from those of the  $\alpha$  phase. Our data also imply the existence of two additional new phases  $\gamma$  at  $x \approx 0.6$  and  $\delta$  at  $x \approx 0.8$  that may be metastable, arising from the highly nonequilibrium ball milling process. All compositions release some ammonia when heated, and those with  $x < 0.667$  (i.e., compositions comprising the  $\beta$  and  $\gamma$  phases) do so at  $T \sim 150$  °C. Compositions near  $x = 0.667$  release the least ammonia and the most hydrogen. All compositions melt and then release hydrogen from the liquid phase at  $T \sim 250$  °C. Melting temperatures determined from XRD data are  $\sim 45$  ( $\gamma$  phase), 75–90 ( $\beta$  phase), 150–190 ( $\alpha$  phase), and  $\sim 50$  °C ( $\delta$  phase). Mixed phase samples showed multiple meltings. A nonequilibrium phase diagram was constructed to show the occurrence of the various crystalline phases, the melting behavior, and the correlation of sample composition and the observed phases with the  $\text{H}_2$  and  $\text{NH}_3$  content of the released gas.

**Acknowledgment.** We thank Laura Confer for assistance with sample preparation and measurement and Matthew Kundrat for assistance with XRD experiments. We also thank Jan Herbst, Stephen Swarin, Mark Verbrugge, and James Spearot for their encouragement and support throughout this research.

## References and Notes

- (1) Pinkerton, F. E.; Wicke, B. G. *Ind. Phys.* **2004**, *10* (February/March), 20.
- (2) Buschow, K. H. J. Hydrogen absorption in intermetallic compounds. In *Handbook on the Physics and Chemistry of Rare Earths*; Gschneidner, K. A., Eyring, L., Eds.; North-Holland: New York, 1984; Vol. 6, pp 1–111.
- (3) Schwarz, R. B. *MRS Bull.* **1999**, *24*, 40.
- (4) Ye, Y.; Ahn, C. C.; Witham, C.; Fultz, B.; Liu, J.; Rinzler, A. G.; Colbert, D.; Smith, K. A.; Smalley, R. E. *Appl. Phys. Lett.* **1999**, *74*, 2307.
- (5) Yang, R. T. *Carbon* **2000**, *38*, 623.
- (6) Pinkerton, F. E.; Wicke, B. G.; Olk, C. H.; Tibbetts, G. G.; Meisner, G. P.; Meyer, M. S.; Herbst, J. F. *J. Phys. Chem. B* **2000**, *104*, 9460.
- (7) Tibbetts, G. G.; Meisner, G. P.; Olk, C. H. *Carbon* **2001**, *39*, 2291.
- (8) Hirschler, M.; Becher, M.; Haluska, M.; Dettlaff-Weglikowska, U.; Quintel, A.; Duesberg, G. S.; Choi, Y.-M.; Downes, P.; Hulman, M.; Roth, S.; Stepanek, I.; Berneir, P. *Appl. Phys. A*. DOI 10.1007/s003390100816, 2001.
- (9) Bogdanovic, B.; Schwickardi, M. *J. Alloys Compd.* **1997**, *253*, 1.
- (10) Meisner, G. P.; Tibbetts, G. G.; Pinkerton, F. E.; Olk, C. H.; Balogh, M. P. *J. Alloys Compd.* **2002**, *337*, 254.
- (11) Balogh, M. P.; Tibbetts, G. G.; Pinkerton, F. E.; Meisner, G. P.; Olk, C. H. *J. Alloys Compd.* **2003**, *350*, 136.
- (12) Gross, K. J.; Majzoub, E. H.; Spangler, S. W. *J. Alloys Compd.* **2003**, *356*, 423.
- (13) Bogdanovic, B.; Felderhoff, M.; Germann, M.; Hartel, M.; Pommerin, A.; Schuth, F.; Weidenthaler, C.; Zibrowius, B. *J. Alloys Compd.* **2003**, *350*, 246.
- (14) Zuttel, A.; Rentsch, S.; Fischer, P.; Wenger, P.; Sudan, P.; Mauron, Ph.; Emmenegger, Ch. *J. Alloys Compd.* **2003**, *356–357*, 515.
- (15) Meisner, G. P.; Pinkerton, F. E.; Meyer, M. S.; Balogh, M. P. *Proceedings of the International Symposium on Metal Hydrogen Systems 2004*, Crakow, Poland, September 8, 2004, and: *J. Alloys Compd.* DOI 10.1016/j.jallcom.2004.11.103.
- (16) Villars, P. *Pearson's Handbook*, desk edition; ASM International: Materials Park, OH, 1997; p 771.
- (17) Goubeau, J.; Anselment, W. Z. *Anorg. Allg. Chem.* **1961**, *310*, 248.
- (18) Wentorf, R. H., Jr. *J. Chem. Phys.* **1961**, *34*, 809.
- (19) DeVries, R. C.; Fleischer, J. F. *Mater. Res. Bull.* **1969**, *4*, 433.
- (20) Yamane, H.; Kikkawa, S.; Horiuchi, H.; Koizumi, M. *J. Solid State Chem.* **1986**, *65*, 6.

- (21) Yamane, H.; Kikkawa, S.; Koizumi, M. *J. Solid State Chem.* **1987**, 71, 1.
- (22) Pinkerton, F. E.; Meisner, G. P.; Meyer, M. S.; Balogh, M. P. *J. Phys. Chem. B* **2005**, 109, 6.
- (23) Filinchuk, Y. E.; Yvon, K.; Meisner, G. P.; Pinkerton, F. E.; Balogh, M. P. *Inorg. Chem.* **2006**, ASAP DOI: 10.1021/ic0518226.
- (24) Pinkerton, F. E.; Meyer, M. S.; Tibbetts, G. G.; Chahine, R. *Proceedings of the 11th Canadian Hydrogen Conference*, Victoria, BC, Canada, 2001; pp 633–642.
- (25) Juza, R.; Opp, K. *Z. Anorg. Allg. Chem.* **1951**, 266, 325.
- (26) Pinkerton, F. E. Decomposition Kinetics of Lithium Amide and its Implications for Hydrogen Storage. In *Mater. Res. Soci. Symp. Proc.* **2004**, 837.

(27) (Vol/TGA) analysis of the volumetric and gravimetric measurements of gas desorption: The total moles of gas desorbed per initial mass of sample, determined by the volumetric measurement, is the sum of the moles of H<sub>2</sub> and moles of NH<sub>3</sub>:  $n_{\text{total}} = n_{\text{NH}_3(\text{g})} + n_{\text{H}_2(\text{g})} = m_{\text{NH}_3(\text{g})}/M_{\text{NH}_3} + m_{\text{H}_2(\text{g})}/M_{\text{H}_2}$ , where  $m_{\text{NH}_3(\text{g})}$  is the mass of NH<sub>3</sub> desorbed per mass of initial sample,  $m_{\text{H}_2(\text{g})}$  is the mass of H<sub>2</sub> desorbed per mass of initial sample, and  $M_{\text{NH}_3}$  and  $M_{\text{H}_2}$  are the molecular weights of NH<sub>3</sub> and H<sub>2</sub>, respectively. The total mass of desorbed gas per mass of initial sample, determined by the TGA measurement, is the sum of the masses of H<sub>2</sub> and NH<sub>3</sub> desorbed:  $m_{\text{total}} = m_{\text{NH}_3(\text{g})} + m_{\text{H}_2(\text{g})}$ . Solving these two equations yields:  $m_{\text{NH}_3(\text{g})} = (m_{\text{total}} - n_{\text{total}}M_{\text{H}_2})(M_{\text{NH}_3}/(M_{\text{NH}_3} - M_{\text{H}_2}))$  and  $m_{\text{H}_2(\text{g})} = (n_{\text{total}}M_{\text{NH}_3} - m_{\text{total}})(M_{\text{H}_2}/(M_{\text{NH}_3} - M_{\text{H}_2}))$ .